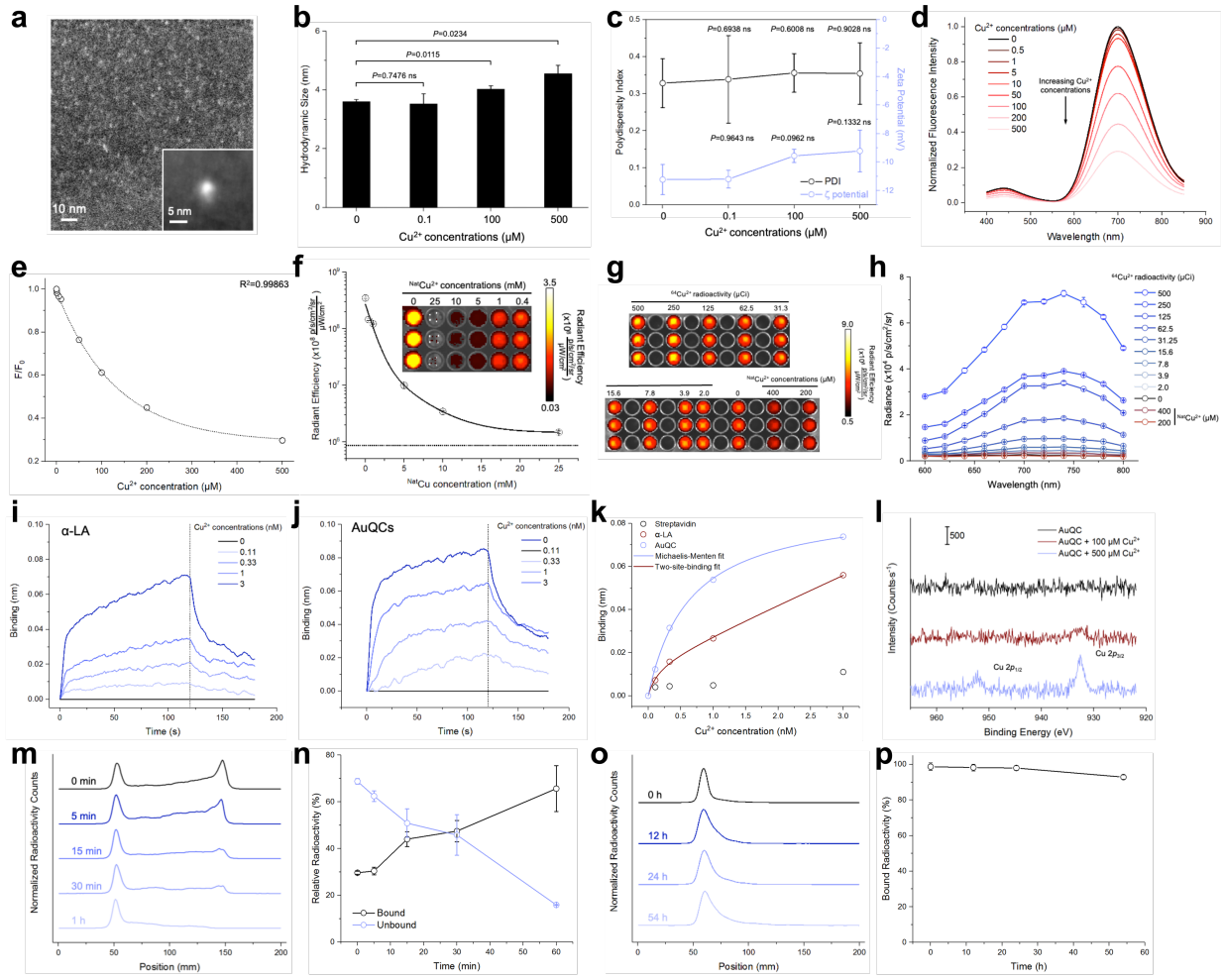

Figure 1: Characterization and room-temperature, chelator-free ^{64}Cu labeling of AuQCs. **a**, Representative STEM images of AuQCs with a magnified individual probe shown in the inset. **b**, Hydrodynamic sizes, **c**, polydispersity indexes and zeta potentials, d, fluorescence emission spectra, **e**, derived NIRF quenching dynamics of AuQCs after interaction with different concentrations of $^{Nat}Cu^{2+}$. NIRF phantom imaging of AuQCs in the presence of gradient concentrations of **f**, $^{Nat}Cu^{2+}$ and **g**, radioactive $^{64}Cu^{2+}$. Corresponding NIRF emission curves for **g** with $^{64}Cu^{2+}$. BLI sensorgrams of **i**, α-LA and **j**, AuQCs in the presence of gradient concentrations of $^{Nat}Cu^{2+}$, resulting in (**k**) distinctly different fitted binding kinetics. **l**, XPS spectra of $^{Nat}Cu^{2+}$-AuQCs in the Cu 2*p* region. **m**, iTLC chromatograms of AuQCs after interaction with $^{64}Cu^{2+}$ for different durations at room temperature. **n**, Quantified relative radioactivity of bound and unbound ^{64}Cu species after different interaction time periods. **o**, Ambient stability of ^{64}Cu-AuQCs by iTLC at different time points. **p**, Time-bound radioactivity correlation as a function of time from the chromatograms in **o**.

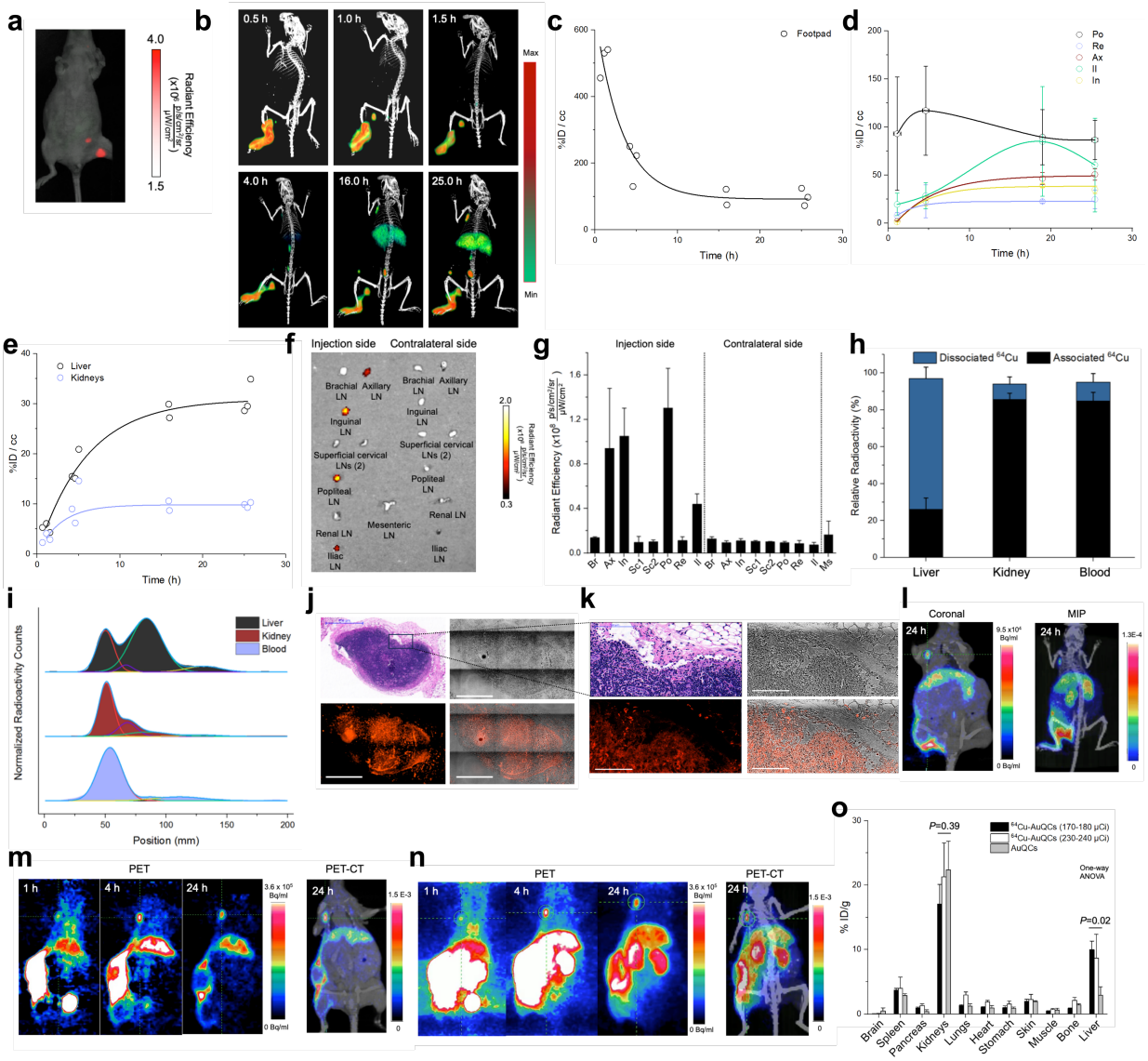

Figure 2: Dual-modality LN imaging by PET and NIRF in living mouse models. **a**, NIRF imaging for detecting draining LNs 1 h after footpad injection of AuQCs in wild-type mice. **b**, PET/CT imaging at different time points following footpad injection of ^{64}Cu-labeled AuQCs in wild-type mice. **c**, The time-activity curve (TAC) of the footpad from PET/CT images for quantitative analysis. **d**, TAC curves of major LNs of axillary, inguinal, popliteal, and iliac LNs with PET signals. **e**, TAC curves of the liver and kidneys. **f**, Ex vivo NIRF imaging and **g**, signal quantification of dissected LNs 1 h post footpad injection. **h**, Quantified associated and dissociated ^{64}Cu species in the liver, kidneys, and blood. **i**, iTLC chromatograms of tissue homogenates from indicated organs. Ex vivo NIRF-imaging and H&E staining of **j**, surgically resected SLN under image guidance and **k**, the magnified region of interest showing LN margins. Coronal and MIP PET/CT images showing LN detection in xenograft mice bearing SCLC PDX tumors **l**, after footpad injection, and **m** and **n**, after peritumoral injection with ^{64}Cu-AuQCs. **o**, Biodistribution of systemically circulating nanoprobes after intravenous injection, calculated by a gamma counter.

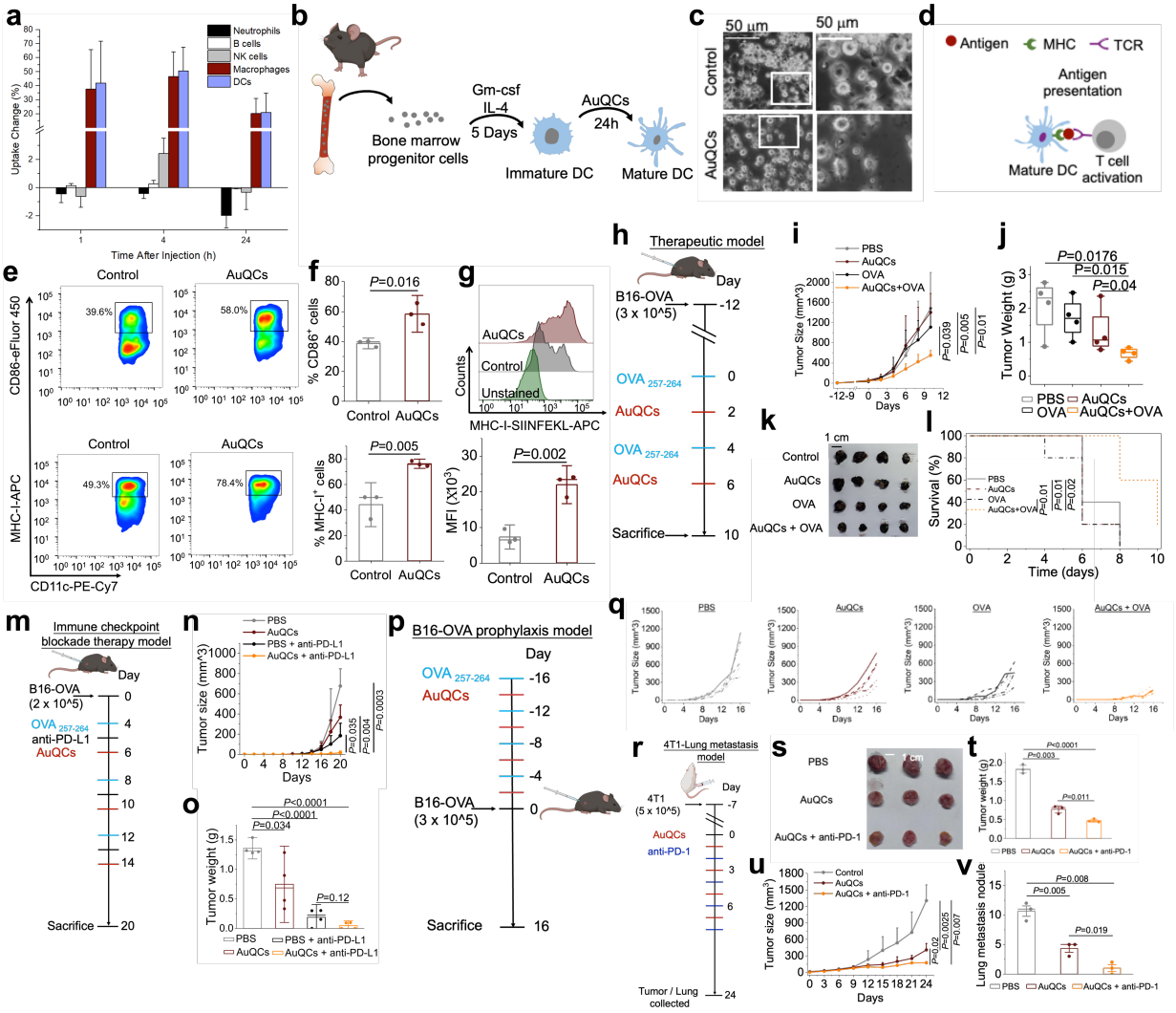

Figure 3: AuQCs as a cancer vaccine. **a**, Uptake of AuQCs in different immune cells in LNs. **b**, A schematic diagram showing the maturation of bone marrow-derived dendritic cells (BMDCs) regulated by AuQCs. **c**, Phase-contrast microscopic images of BMDCs with or without treatment of AuQCs. **d**, A schematic diagram showing the antigen-presenting process to naïve T cells by DCs. **e**, Flow cytometry analysis of maturation and antigen presentation of DCs influenced by AuQCs. **f**, Quantitative analysis of matured DC and APC populations. **g**, Flow cytometry analysis of MHC class I presented antigen levels. **h**, The experimental scheme evaluating AuQCs as a cancer vaccine for therapy in B16F10-OVA allograft mouse models. **i**, Tumor growth curves, **j**, tumor weights, **k**, the photograph of tumors, and **l**, survival curves of allograft mice receiving therapeutic cancer vaccines of AuQCs and $OVA_{257-264}$. **m**, The experimental scheme using AuQCs vaccines in combination with anti-PD-L1 ICI therapy. **i**, Tumor growth curves and **j**, tumor weights harvested from allograft mice. **p**, The experimental scheme using AuQCs as a prophylactic cancer vaccine. **q**, Individual tumor growth curves in different groups of B16F10-OVA allograft mice. **r**, The experimental scheme using AuQCs as vaccines in combination with anti-PD-1 antibody ICI therapy in 4T1 allograft mouse models. **s**, The

photograph, **t**, tumor weights, and **u**, tumor growth curves of primary orthotopic tumors. **v**, Quantification of metastasized lung nodules.